Volume Raycasting of GNSS Signals through Ground Structure Lidar for UAV Navigational Guidance and Safety Estimation

Andrew J. Moore[1], Matthew Schubert[2], Nicholas Rymer[3], Daniel Villalobos[4], J. Sloan Glover[5], Derin Ozturk[6] and Evan Dill[7]

NASA Langley Research Center, Hampton, VA

Autonomous UAS navigation at low altitudes is often hindered by degradation of GNSS position estimates. The line of sight from the UAS to orbital satellites may be intersected by foliage (which attenuates the received signal) and by buildings (which block the signal). Since the geometric ray from the presumed UAS position to each GNSS satellite orbital location is predictable, if a 3D survey of ground structures is available, the degree of blockage of each GNSS signal can be estimated. In this study we show raycasting from a UAS location to GNSS satellites at two flight locations: one with overlying structures and bordered by tall trees, and another in an arboreal canyon bordered by tall trees. We confirm the intermittent blockage of satellites in the first location sufficient to lose GNSS position fix. We demonstrate low-altitude GNSS fidelity forecasting via the raycasting method at the second location that can be used to plan navigable flight locations and altitudes. Finally, we match the GNSS signal strength with raycast-derived foliage obstruction depth at hundreds of observation times from 55 recordings collected over 14 days from November 2018 to February 2021 at the second location. This matching confirms that signal attenuation varies with the depth of foliage blockage along a saturating exponential curve, as found in prior continuous-wave radio studies. The exponent and saturation value are species dependent and therefore vary from site to site; once determined empirically, they can be used to characterize foliage along a particular flight path and refine GNSS fidelity forecasts of flights along that path. The techniques described in this study show the feasibility of a survey method to construct low-altitude navigation safety maps and forecasts.

I. Nomenclature

AGL	=	altitude above ground level
c/N0	=	GNSS signal carrier to noise ratio
ECEF	=	earth-centered-earth-fixed coordinate system
EKF	=	extended Kalman Filter
FIPS	=	Federal Information Processing Standard
GLONASS	=	Global'naya Navigatsionnaya Sputnikovaya Sistema
GNSS	=	Global Navigation Satellite System
GPS	=	Global Positioning System
HARN	=	High Accuracy Reference Network
NAD83	=	North American Datum of 1983
UAS	=	Unmanned Aerial System
UAV	=	Unmanned Aerial Vehicle

---

[1] Aerospace Research Engineer, Dynamic Systems and Control Branch
[2] Research Engineer, Analytical Mechanics Associates, Inc.
[3] Research Engineer, National Institute of Aerospace
[4] Graduate Student, University of Maryland
[5] Research Engineer, Analytical Mechanics Associates, Inc.
[6] Graduate Student, Georgia Institute of Technology
[7] Aerospace Research Engineer, Safety-Critical Avionics System Branch, Member

UTC   =   Coordinated Universal Time
WGS84   =   World Geodetic System 1984

II. Introduction

Autonomous UAV (Unmanned Aerial Vehicle) navigation at low altitudes amongst foliage and ground structures is often hindered by degradation of GNSS (Global Navigation Satellite System) position estimates. The line of sight from the UAS (Unmanned Aerial System) to orbital satellites may be intersected by vegetation (which attenuates the received signal) and by buildings (which block the signal). Since the geometric ray from the presumed UAV position to each GNSS satellite orbital location is predictable at a given time and position on the earth's surface, and if 3D lidar of ground structures is available, then the degree of blockage of each GNSS signal can be estimated. These blockage estimates can be used to create navigation safety maps, to refine UAS position estimates, and to beneficially control navigation.
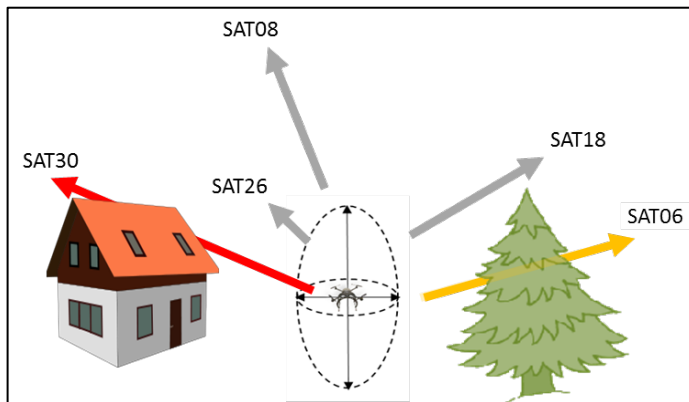
This study presents a method to quantify direct-path (from the UAV to the satellite) GNSS quality using survey lidar of ground structures and foliage. The method can potentially provide a measure of waypoint stability over time, and so may be used to plan navigationally reliable flight paths. It may also be used during flight to adjust the vehicle altitude to a height with a superior GNSS position fix. Lastly, the method can provide a tool for post-flight analysis to diagnose the degree of positional uncertainty.

The method corresponds to volume raycasting in computer graphics [1] and computed tomography [2], in which paths from a viewpoint to points of intersection with objects in a scene are found and samples of the object density each path travels through the object are estimated to form a measure of transparency between the viewpoint and the scene boundaries. The more compute-intensive (and visually realistic) raytracing technique in computer graphics [3] additionally computes reflections from the object surface to other objects and light sources. Since reflections of orbital GNSS signals from the ground or from nearby structures and foliage (called multipath signals [4][5]) are not considered in the method used in this study, it is more analogous to raycasting than raytracing. Since scattering around structures and reflections from specular surfaces are not considered, this method employs a simplified geometric optics model [6]. Limitations of the method are described in the Discussion section.

Previous studies have used similar geometric approaches to model the navigational quality of GNSS position, primarily for ground-based receivers. GNSS signal blockage estimation in the literature has ranged in geometric complexity from manual tracing of select structures [6] to raycasting with a small number of solid models in a 3D scene of ground structures [5][7][8][9] to raycasting in urban canyons using rich lidar data [10]. Two recent studies have shown that limited raytracing can be used to include satellites in the positioning computation which are not in direct line of sight of the receiver [11][12].

Fig. 1 Tracing the ray blockage from a UAS to five orbital satellites. The left ray is completely blocked (red), the right ray is attenuated (yellow), while the remainder (grey) are free of intersection with ground structures. ©*Graphics: NASA, NOAA, USDA*

Aerial and ground-based lidar surveys of structures and foliage are increasingly undertaken for several applications such as ecology and forestry [13], power line management [14] and inspection [15][16], and urban mapping [17].

The computational effort required to estimate GNSS accuracy with full geometric rigor using detailed terrain data is considerable. In the course of this investigation, two other [10][11] studies have been published that similarly attempt complete geometric fidelity; the emergence of multiple independent inquiries into a higher understanding of navigational accuracy at low altitudes bodes well for the broad navigation community.

III. Raycasting Method

The method is shown schematically in Figure 1. The paths from a GNSS receiver (here shown as a small UAV) to each GNSS satellite (SAT06, SAT08, etc.) overhead is traced and ground obstructions along each path are used to estimate signal attenuation. Paths that are clear of obstruction are assigned 0% attenuation (grey rays), paths that are obstructed by structures are assigned 100% attenuation (red ray), and paths that are obstructed by foliage are assigned

intermediate attenuations (yellow ray). As the GNSS satellite constellation moves across the sky, raycasting and attenuation assignment is updated at each instant of receiver position estimation (typically once per second). In this report, a measure of GNSS degradation is computed using this method at two flight ranges.

A. Flight Ranges and Survey Lidar

The method was applied using survey-grade lidar of two GNSS degraded locations at the NASA Langley Research Center. The first location, shown in Figures 2 and 3, is the site of the Lunar Lander Research Facility. At this location,
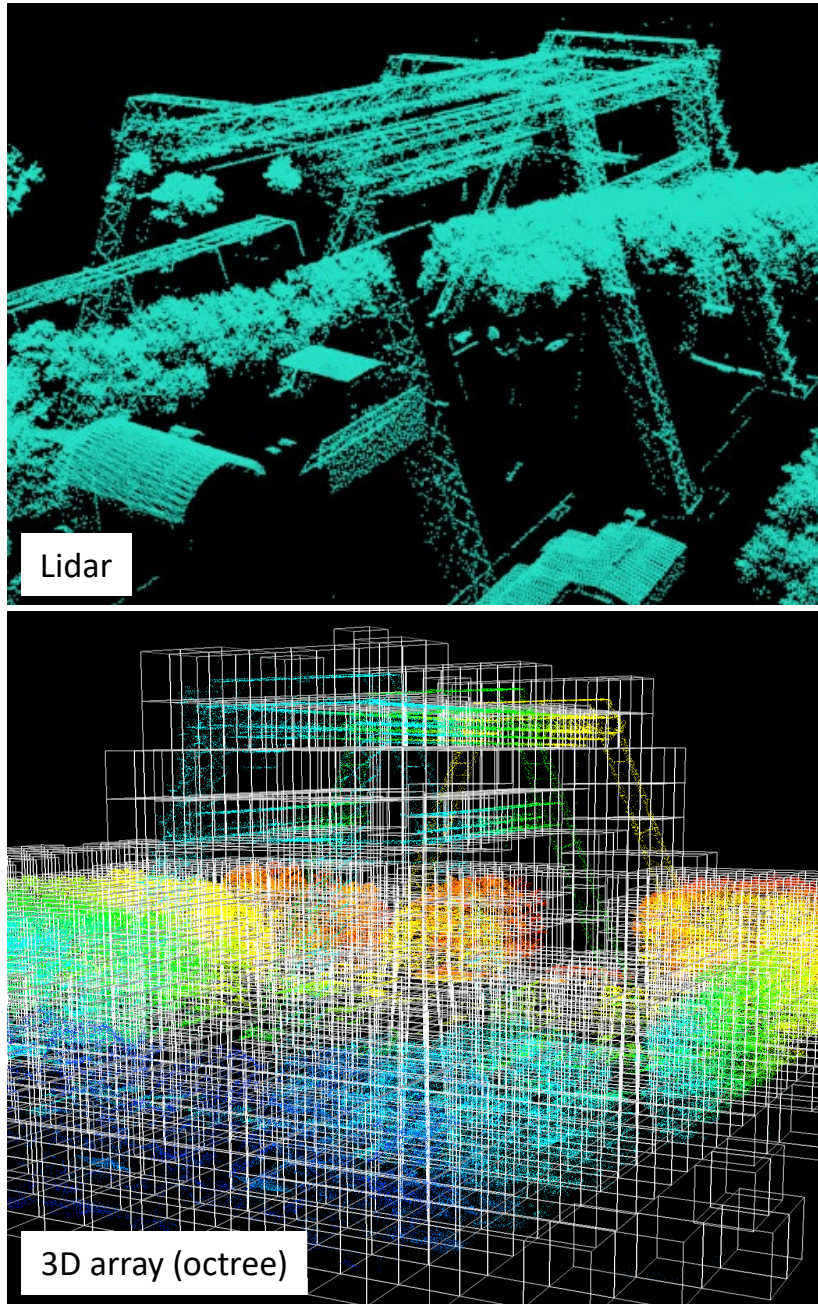
Fig. 2 Aerial scan lidar of Lunar Lander Research Facility structure (top) and octree representation with color assigned according to altitude (bottom). The voxel size shown is coarser than the actual computational voxel size of 0.5m on a side. ©*Map data: NASA*

several buildings and trees surround a steel structure ('the gantry') 70 m in height with dimensions 92 m north-to-south by 195 m east-to-west at its base and 32 m north-to-south by 120 m east-to-west at its top. GNSS positioning at this location is degraded at ground level and low altitudes due to blockage and attenuation by the gantry and tree cover.

Aerial lidar of the site was gathered in 2015 at an average point spacing of 17 cm. It was prepared for raycasting as follows: (1) lidar points in the ground plane were removed (Figure 2, top); (2) the nonground points were recast from their original coordinate system (State Plane Virginia South, NAD83 HARN, FIPS 4502; where NAD83 is North American Datum of 1983, HARN is High Accuracy Reference Network, and FIPS 4502 is Federal Information Processing Standard location 4502) to the coordinate system used for GNSS satellite orbits (ECEF, WGS84; where ECEF is Earth Centered Earth Fixed and WGS84 is World Geodetic System 1984); (3) a georeferenced facilities database was used to classify each lidar point above ground as arising from either foliage or from a building/structure; and (4) foliage and building lidar were separated and stored separately as two aligned sets of point clouds f and b. The two lidar point cloud sets were then read separately into Point Cloud Library (PCL, [18]) and organized into aligned 3D octree voxel arrays V_f and V_b in the ECEF coordinate system with a voxel size of 0.5 m³. The arrays are shown in the merged PCL view at the bottom in Figure 2, with the voxel grid (white lines) coarsened to 10 m³ to reduce presentation clutter and false color shuffled slightly from voxel to voxel to aid in visualization.

The second location is a portion of a steam pipeline corridor. At this location, tall (20 m) trees abut a cleared area 13 m wide and 75 m long. This cleared area forms an arboreal canyon within a forest comprised of mixture of hardwood species (primarily sweetgum, oak and sycamore). The pipeline is centered in the cleared area and rises up to 2 m above ground. GNSS positioning at this location is degraded at ground level and low altitudes due to attenuation by foliage. The site is free of buildings and structures, except for the pipeline. Blockage by distant buildings and the pipeline is disregarded in the analysis at this site.

Two lidar surveys are used for the second (pipeline) site: (1) aerial lidar at an average point spacing of 10 cm gathered in 2018 and (2) ground lidar with an average point spacing of 8 cm gathered in 2018 from merging scans taken at two surveyed ground points in the pipeline corridor. The aerial survey was conducted in partial foliage conditions (spring: March 28, 2018) and the ground survey was conducted in partial foliage conditions (autumn; Nov 20, 2018, before leaves had fully dropped). After processing to remove points in the ground plane, the aerial and ground survey coordinates were projected into an ECEF coordinate system.

B. Calculation of Attenuation Along Ray Paths

For each time t of a given GNSS positioning record, a set of n rays $\overrightarrow{LH}$ is constructed, originating from a low-altitude point L to one of n high-altitude points H (the orbital satellite position). The point L is taken as the reported position. The point H is taken as the orbital position of each satellite at time t, obtained from NASA's Archive of Space Geodesy Data [19]. Both GPS (United States Global Positioning System) and GLONASS (Global'naya Navigatsionnaya Sputnikovaya Sistema) GNSS constellations were used throughout this study.

A C++ program using the PCL library (version 1.7.2) of point cloud functions finds all voxels $V_{LH,i}$ in each array intersected by a ray $\overrightarrow{LH}$ at time t and records an attenuation value $\alpha(V_i)$ for each intersected voxel V_i. Attenuation values are assigned on a per-array basis. Voxel attenuation values $\alpha_{b,i}$ for the building array V_b are set to 1.0 (100%) if the voxel contains any lidar points from buildings. Voxel attenuation values $\alpha_{f,i}$ for the foliage array V_f are set to a coarse estimate of 0.1 (10%) if the voxel contains any lidar points from foliage. (While this 10% foliage estimate is sufficient to visualize the phenomenology of GNSS degradation, better estimates can be found empirically; see *Characteristic Curve of Foliage Attenuation* section below). The C++ program computes, for each ray at time t, the collection of intersected voxels and their attenuation values. Computed attenuation values are then summed to obtain a total attenuation α_{LH} for each ray at time t.

$$\forall \overrightarrow{LH}(t): V_{LH,i} = \left(V_f \cap \overrightarrow{LH}(t) \right) \cup \left(V_b \cap \overrightarrow{LH}(t) \right) \tag{1}$$

$$\alpha_{LH} = \alpha_{LH,f} + \alpha_{LH,b} \tag{2}$$

$$\alpha_{LH} = \sum_i \alpha_{f,i} + \sum_i \alpha_{b,i} \tag{3}$$

The degree of signal blockage for each ray was visualized (Figure 3, Figure 4) by coloring it according to its attenuation value: grey for attenuation below 10% (no blockage of the satellite signal by structures captured in the lidar survey), yellow for attenuations from 10% to 40%, orange for attenuations from 50% to 99%, and red for attenuation equal to or greater than 100%. The total attenuation α_{LH} is allowed to exceed the physical limit of 100% attenuation, e.g., in the rare case that the path intersects both building and foliage lidar points.

For the first site, both foliage and building attenuations were computed. Since the second site is distant from buildings, the building V_b is empty, so that only foliage attenuations $\alpha_{LH,f}$ were computed.

IV. GNSS Raycasting At Two Sites

A. Application at Lunar Lander Research Facility Site

Walking surveys were conducted a few minutes apart on 2017/01/19 beneath the Lunar Lander Research Facility gantry on a fixed cruciform path. First, the georeferenced endpoints of the two perpendicular arms of the ground path (18 m north-south and 18 m east-west segments) were obtained via long (several hour) baseline measurements using a


16:07-16:13

16:13-16:14

16:25-16:28
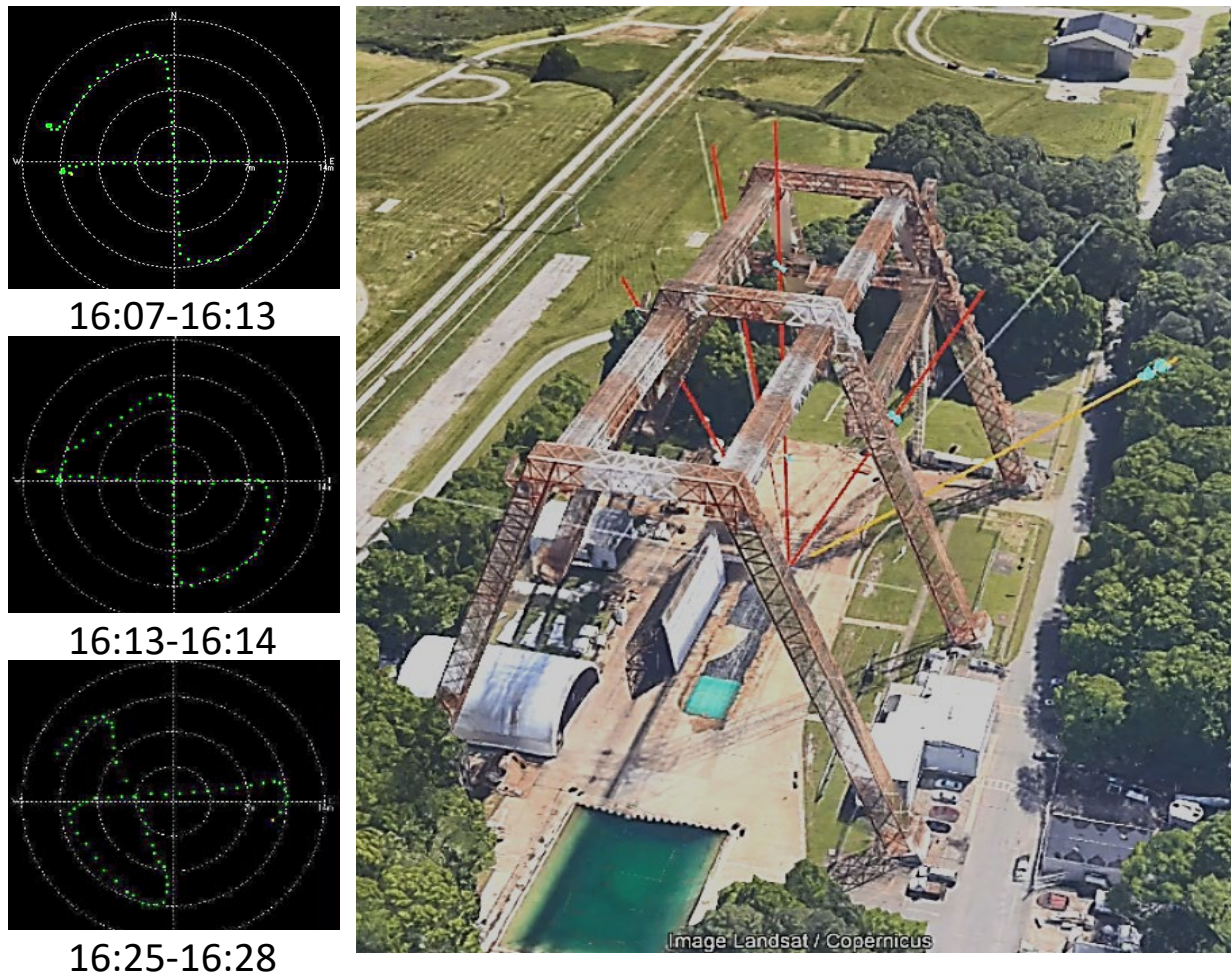
Fig. 3. Ground surveys and research flight conducted under Lunar Lander Research Facility structure. Left: Walking surveys conducted a few minutes apart on 2017/01/19 beneath the structure on a fixed cruciform path (18m north-south and east-west segments) showed accurate position determination sometimes (green dots in top two plots; good alignment with compass directions) but severe deviations from ground truth at other times (green dots in bottom panel). Traversal times are shown in hour:minute format; outer radius is 14m. Right: At the instant shown during a flight on 2018/01/15, five of the eight paths to orbital GPS signals are blocked completely (red rays) or partially (yellow ray). Blockage of orbital satellites by ground structures demonstrated by raycasting at right explains the intermittent deviations found in the walking surveys at left. ©*Map data: Google*

u-blox[TM] M8P receiver[8]. Next, the stability of positioning quality at this site was explored by walking the path segments with a 'rover' receiver paired to a fixed 'base station' receiver (u-blox[TM] C94-M8P kit). Three representative results taken a few minutes apart are shown at left in Figure 3. While the real-time position matched ground truth positions most of the time (green dots in top two panels), severe deviations were observed intermittently (green dots in bottom panel). The survey times are shown in hour:minute format. Intermittent dropout of some satellites is to be expected as overhead satellites are blocked by the steel I-beams of the Lunar Lander Research Facility gantry. Spot checks of the GNSS constellation skyplot during these walking surveys suggested that a satellite was passing through 90° elevation and subject to shadowing by the overhead gantry cross beams during the survey period.

A flight study was conducted at the site in January 2018, and archived telemetry was analyzed with the raycasting method. Flight test positioning was determined from a commodity navigational GNSS receiver (u-blox[TM] NEO-M8N module) on a UAV. This M8N module reports a position (latitude, longitude, and altitude) after smoothing by an onboard Kalman filter. It also reports the count of satellite signals available for computing a position fix and fix quality metrics. It does not record the satellite identification numbers of available GNSS signals or which received signals are used to compute a position fix. The UAV was equipped with a Pixhawk[TM] autopilot running Ardupilot[TM] ArduCopter (v3.5.3) autopilot software, which combines the M8N positioning data with the autopilot's compass, IMU (inertial measurement unit), and barometer sensor data via an Extended Kalman Filter (EKF) to form the autopilot positioning telemetry. The M8N module was configured (by default autopilot settings) to reject signals from satellites below 5° in elevation.

In some flights, the UAV was launched from a point underneath the gantry and flown vertically to altitudes well above the height of the structure. In other flights, the UAV was launched from the same location and flown to an altitude well below the top of the gantry structure and then laterally to positions outside of the structure in both north-south and east-west directions. All UAV telemetry was archived for further analysis.

For each time t of flight, point L was taken as the position reported by the navigational GNSS receiver and filtered by the autopilot EKF. The orbital positions of each GPS and GLONASS satellite at time t were read from NASA's CDDIS (Crustal Dynamics Data Information System) archive [19]. For each satellite above 5° elevation at time t, point H was set as its orbital position and the attenuation along the ray $\overrightarrow{LH}$ was calculated as described above. The results for a representative instant of flight time are shown at right in Figure 3. In this instant, the UAV is beneath the Lunar Lander Research Facility gantry structure and of the eight GNSS satellites above 5° elevation, four are completely blocked by the structure and one is partially attenuated by foliage. Only four GNSS signals are available
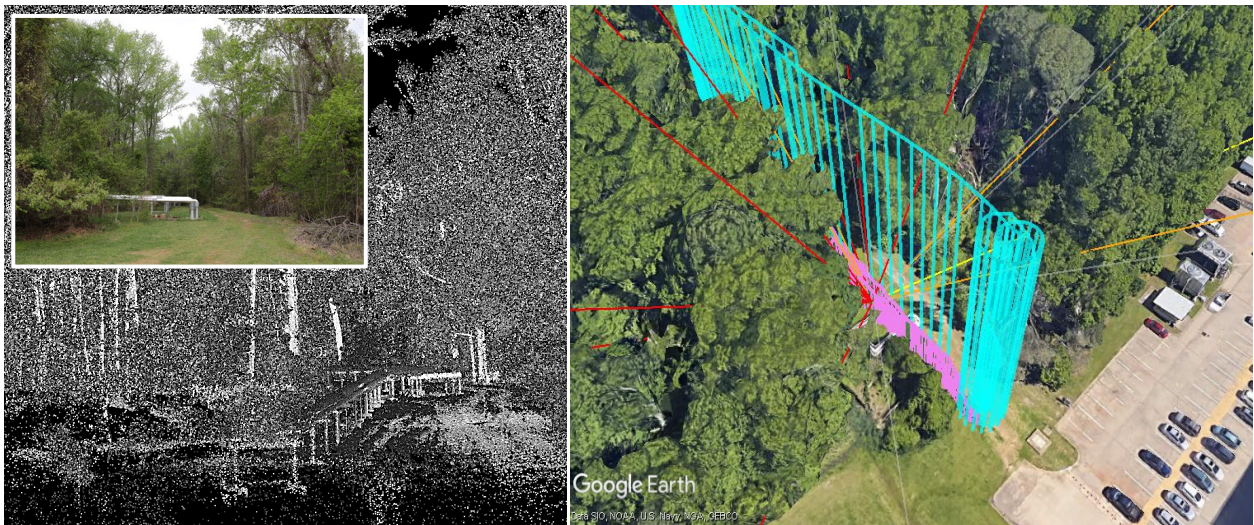
Fig. 4. Flight range in arboreal canyon. Left: Ground scan lidar and (inset) photo of flight range with steam pipeline structure. Right: Trajectory of 40m (cyan) and 5m (pink) flights on 12/14/2018 with raycast to orbital satellites at one time instant of the 5m flight. The raycast coloration assumes 10% attenuation for each voxel in the ray path. ©*Map data: Google, NASA*

---

[8] The use of trademarks or names of manufacturers in this report is for accurate reporting and does not constitute an official endorsement, either expressed or implied, of such products or manufacturers by the National Aeronautics and Space Administration."

for position calculation, and one of the four is attenuated by foliage, so instantaneous position determination is subject to error. This raycasting analysis confirms the intermittent nature of position determination at this site as observed in the walking surveys.

B. Application at Pipeline Corridor Site

Like many infrastructure corridors, the steam pipeline corridor at NASA Langley Research Center is an arboreal canyon bounded by tall, thick woods with no nearby buildings. Because GNSS signals are typically only attenuated (but not blocked) by foliage, it is contrary to intuition that complete loss of positioning can occur, and not obvious why such loss is intermittent. On more than one occasion in low altitude UAS operations in such corridors [15][16][20], we attributed loss of navigation to a hardware problem, and commenced troubleshooting — only to find that acceptable navigation fidelity resumed in a few minutes. Of course, the physical explanation was that as the GNSS constellation moved across the sky, the number of satellite signals severely attenuated by foliage varied. Most of the time there were enough good signals reaching our position in the arboreal canyon that positioning sensors could compute a good 3D fix, but occasionally the geometry of the canyon and constellation was not so fortunate.

To illuminate the variation in GNSS navigation quality in arboreal canyons, we took three approaches to the application of the raycasting method. First, we directly applied the postflight visualization used at the gantry site. Second, we implemented a visualization tool that accepts a set of precomputed raycast results to forecast navigation quality at multiple times and altitudes. For these first two approaches, attenuation coefficients $\alpha_{LH,f}$ were assigned nominal values. Third, we measured actual attenuation across multiple days, seasons, and altitudes to permit exact computation of navigation quality. In this section we report on the first two approaches and describe initial results for the third approach.

1. Postflight visualization

Figure 4 shows lidar of the pipeline corridor and visualization of GNSS signal reception for a low altitude position in the corridor. As for the gantry site, the lidar is arranged as a 3D array of voxels with edge length 0.5m, rays are cast from the corridor location to each satellite, and the attenuation coefficient is set to 10% per intersected voxel. Intersected voxel attenuations are summed along each ray, and the ray is colored on a scale ranging from grey to red. This visualization approach enabled matching of the spatial coordinate systems and time bases of each of the experimental datatypes (autopilot log, GNSS sensor log, lidar survey).

2. Forecasting navigation fidelity across time and altitude

Navigation fidelity estimation and forecasting is an essential requirement for safe low-altitude aviation [21]. To prototype this function, we ported the raycasting software to a standalone Linux virtual machine and implemented a more versatile visualization based on ArcGIS Online. This prototype (Figure 5) accepts a flight plan (series of locations), a set of candidate flight times, and a range of flight altitudes in a web-based form. As the raycasting may take several minutes of compute time, the system provides a unique forecast identification number upon acceptance of the flight plan and forecast times, and computes the raycast results. Once complete, a flight planner may browse the forecast results interactively.

Figure 5 shows a forecast computed on a virtual machine running at Katherine Johnson Compute Facility at the NASA Langley Research Center with 12 CPU cores and 42 GB RAM. The 1.1 GB lidar array covers the wooded area to a distance of approximately 200 m on either side of the corridor and is organized as 11 million voxels (0.5 m on a side). Ten flight waypoints separated by 30-50 m along a 350 m flight path are simulated at five AGL (above ground level) altitudes (0 m to 40 m in 10 m increments) at thirteen times (10 minute intervals over a 2 hour period) using GPS and GLONASS constellations. This forecast of 650 fidelity estimates was computed in 52 seconds.

A time slider (at bottom in Figure 5) provides selection of one of the forecast results among the eleven time points. Times are shown in Coordinated Universal Time (UTC). Altitude may be selected (slider at right in Figure 5) from ground level to 40 meters in increments of 10 meters. In the example shown, foliage attenuation is set to 100% per intersected voxel, and only satellites with no obstruction are counted. A marker at each location is colored according navigation quality, based on the unobstructed satellite count (red: $0-5$; yellow: $6-8$; green: $9-11$; gray: 12+). In this rather pessimistic estimate, the forecast shows that the flight path at 10 meters altitude is unnavigable at the second waypoint, which is 80 meters inside the canyon (red marker labeled as waypoint 4, inset of Figure 5).

This visualization tool accepts arbitrary per-voxel attenuation coefficients $\alpha_{LH,f}$, and at less pessimistic values the fidelity varies over time, as the GNSS constellation changes to geometries that are better or worse for reception deep in the arboreal canyon. The flight planner can thereby choose altitudes and flight time to optimize navigation. In infrastructure inspection within such corridors, there is great value in flying low to the ground to capture the best inspection imagery; however, the tradeoff between inspection quality and navigability is complex and varies with time. Therefore, this prototype is built to allow a flight planner to explore the tradeoff within a particular flight time window.

Fig. 5. Forecast of GNSS positioning quality in arboreal canyon. Waypoints along the steam pipeline flight range are raycast to the changing GNSS constellation. The slider at right selects altitude offset from the input flight path and is set to 0 m offset from a ground level input altitude in this image. The slider at bottom selects time in 10 minute intervals. In this forecast, any blockage along the ray is assumed to completely block the satellite. The number of unblocked satellites is tallied and assigned a thermometer color ranging from red to green to grey. Inset: Closeup of the four easternmost waypoints, numbered from east to west. The launch point at right (waypoint 1) receives 12 satellites without attenuation while deep in the canyon at left less than 5 satellites are in clear line of sight. ©*Map data: NASA*

3. Empirical determination of GNSS signal attenuation by foliage

Attenuation coefficients for foliage at GNSS frequencies are not broadly characterized. Few studies [22][23][24] attempt systematic methods of measurement needed to ascertain them; further, the radiofrequency propagation models and units of attenuation differ among them. The modeling framework and units of measurement used here follow those of the United Nations' International Telecommunication Union (ITU) [22].

Characteristic Curve of Foliage Attenuation

A complete physical model of foliage attenuation of radio waves requires knowledge of the foliage species and spatial distribution with respect to a radio transmitter and receiver, and accounts for diffraction and lensing effects [22]. To a second-order approximation, attenuation along a direct path between transmitter and receiver increases with canopy depth D as a saturating exponential of the form $a(1 - exp(-b \cdot D))$. In particular, attenuation by foliage A_f may be approximated as

$$A_f = A_m \left[1 - exp \left(- D \gamma / A_m \right) \right] \tag{4}$$

where maximum attenuation A_m and incremental path attenuation γ both increase monotonically with frequency. The shape of this characteristic attenuation curve varies with species and varies seasonally with leaf thickness; empirical values have been determined for some frequencies and species for narrowband, continuous-wave RF. For representative vegetation (mixed forest in Mulhouse, France with height and density similar to our experimental ranges) and radio frequency of 1.5 GHz (close to the GNSS L1 frequency), the curve saturates (A_m) at path lengths of about 200 m at approximately 27 dB attenuation. At 1.2 GHz (close to the GNSS L2 frequency), the curves saturate slightly lower at about 25 dB. Values for γ on the order of 0.3 dB/m can be found by interpolating a plot of typical path attenuation [22] (L1: 0.315 dB/m; L2: 0.246 dB/m) to plot reference continuous-wave foliage attenuation curves (Figure 6, left).

Empirical GNSS Signal Foliage Attenuation

GNSS signals are not narrowband (GPS L1 Band: 1575.42 MHz with a bandwidth of 15.345 MHz; GPS L2 Band: 1227.6 MHz with a bandwidth of 11 MHz) and are so weak that continual autocorrelation and averaging is required to recover the weak satellite signal from noise [25]. Further, GNSS receiving antennas such as the patch antennas used in this study are smaller than the quarter-wavelength dipole antennas used in continuous-wave reference studies. As a result, the values A_m and γ would be expected to differ for GNSS signals as compared to the narrowband values.

8

Empirical determination is possible in principle by matching foliage density determined by the raycast method with observed GNSS signal strengths.

To pursue this approach, a second GNSS receiver was employed that records the entire positional data stream (satellite ID, orbital position, pseudorange, etc.) during traversal in the steam pipeline corridor. Recordings were collected on fourteen days spanning two winter seasons (Table 1). On a typical experimental day, five datasets were collected: two at 40 m altitude above the trees, two at 5 m altitude inside the canopy, and 1 at ground altitude (shown as 1 m AGL in Table 1). Rays from one representative point are shown at right in Figure 4. The ground altitude measurements were obtained by hand-carrying the receiver along the path, while higher altitude measurements were obtained by attaching the sensor module to a UAV.

Table 1 Experiments in Arboreal Canyon. GNSS L1 signals were recorded on all dates. L2 signals were also recorded where indicated.

Date	L1 Records	Altitude AGL	L2 Records
2018_11_02	2	1m	
2018_11_07	4	40m,30m,20m,10m,5m	
2018_11_21	3	40m, 5m, 1m	
2018_12_06	4	40m, 5m	
2018_12_14	6	40m, 5m, 1m	
2019_01_28	2	1m	
2019_02_28	6	40m, 5m, 1m	
2019_03_14	5	40m, 5m, 1m	
2019_04_04	5	40m, 5m, 1m	
2019_04_12	1	1m	
2019_04_19	1	1m	
2020_11_04	6	1m	3
2020_11_27	6	1m	2
2021_02_10	5	1m	2

A receiver that collects L1 signals (u-blox NEO-M8T) was used on all days, and a second receiver that collects both L1 and L2 signals (u-blox™ ZED-F9P) was used on the three experimental days in 2020 and 2021. As with the M8N navigation receiver, the patch antenna feeding the sensors was mounted on a 10 cm by 10 cm square ground plane. A total of 55 recordings were collected, 48 of L1 signals and 7 of L2 signals. The NEO-M8T sensor collected the bulk of these (48 recordings). To allow airborne sensing, the NEO-M8T sensor was encapsulated into a module with an Arduino™ Teensy, which captured the sensor output and saved it to nonvolatile SD card storage. Unlike the M8N navigation receiver, the M8T and F9P modules were not configured to reject signals from satellites below 5° in elevation. Since signals from satellites near the horizon suffer the greatest attenuation by foliage, data from low elevation satellites is especially significant in this method.

 The satellite signal strengths were retrieved by post processing the sensor data with RTKLIB (version 2.4.3/demo5/b31 [26]) and compared with the foliage depth along the ray from the sensor position to each satellite. A set of custom bash scripts was developed to compute the postflight position with RTKLIB. Both a single sensor solution and a differential solution were computed. For the differential solution, stationary GNSS sensors close to the flight range served as the base station. Since RTKLIB removes weak (less than 10 dB) signals from its the position solution, care was taken to retain signal strength observations from these 'dropped satellites' along with observations above 10 dB. These weak observations are important because they are usually from satellites low in elevation and highly attenuated by foliage.

Matching of signal strength and raycast results was verified by comparing the computed postflight position and the in-flight position reported by the navigational M8N GNSS sensor (as refined by the ArduCopter autopilot EKF) for several recordings. This eliminated several sources of systematic mismatch between comparison inputs, including temporal (between GPS time and UDT, and between the ground control station laptop time and UDT) and geometric (altitude reference of the lidar dataset, autopilot position, and GNSS base station) discrepancies. A set of custom Python scripts applied the necessary temporal and spatial offsets and matched the raycast foliage depth results with the measured signal strengths.

Figure 6 depicts the attenuation curve for typical values of saturation attenuation A_m and incremental path attenuation γ for narrowband, continuous-wave RF of 1.2 GHz and 1.5 GHz at left (from [22]), and experimental results for GNSS L1 and L2 signals at right. Composite overlays of all L1 results and all L2 results are shown at top right, and representative single experiment results are shown at bottom right. A fit of a curve of the form of Equation 4 to the

experimental data provides empirical estimates of A_m and γ. The A_m values are comparable: 26 dB for continuous-wave 1.5 GHz RF *vs.* 33-35dB for GNSS L1; 24 dB for continuous-wave 1.2 GHz RF and 30-31 dB for GNSS L2. As the carrier frequency for L2 (~1.2 GHz) is lower than L1 (~ 1.5 GHz), and A_m increases with frequency, this result conforms with the physical model.

The values of path loss γ found in our results (~3 dB/m) are a factor of 10 higher than the typical values found in continuous-wave characterization studies (~ 0.3 dB/m). Fitting a curve to this noisy experimental data is inexact, but this cannot explain a factor of 10 departure from the continuous-wave result. We surmise that it arises from the difference in transmission and reception of the two techniques. The measurements reported by the ITU employ narrow band, continuous wave transmission and reception. The difference between transmitted power and received power is clearly due to attenuation. In contrast, observed GNSS signal strength is not expressed as received power but as a ratio (c/N0, carrier to noise ratio), GNSS transmissions range over band spread (15 MHz for L1 and 11 MHz for L2), and reception is based on continual autocorrelation and averaging.
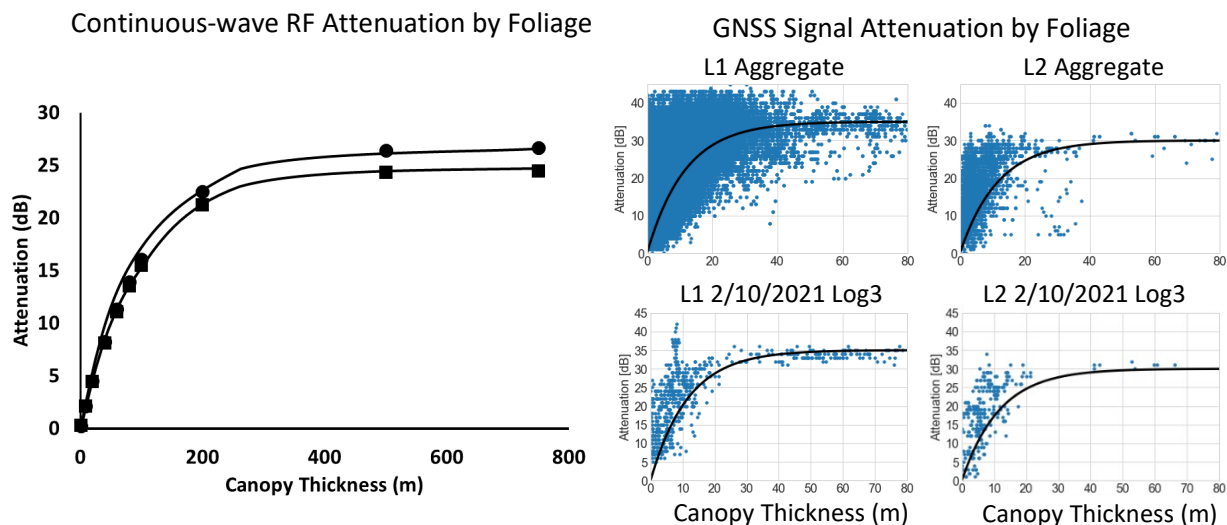
Fig. 6. Left: Attenuation vs. foliage depth. Left: Characteristic curve plotted using typical values for narrow band, continuous-wave signals at 1.5 GHz (circles) and 1.2 GHz (squares) (from [22]). Right: Characteristic curves determined from experimental recordings after matching raycast foliage depth matching to receiver signal (c/N0) in the pipeline arboreal canyon. L1 results are shown in the left column, with an overlay of 48 L1 results at top and a representative single measurement from February 10, 2021 at bottom. L2 results are shown in the right column, with an overlay of 7 L2 results at top and a representative single measurement at bottom.

V. Discussion

A. Limitations of the Method

Due to physical, measurement, and computational simplifications, the estimates of attenuation yielded by this method should be considered indicative rather than exact. First, the method greatly simplifies the physics of GNSS reception near ground structures. It does not consider the reflection of satellite signals from the ground and from structures and foliage (multipath signals) or diffraction/lensing of signals by structures and foliage. For example, at the pipeline site, ray blockage and reflection by distant buildings and the pipeline is disregarded in this initial analysis; this would produce spurious attenuation-opacity points in the plots in Figure 6. Second, it assumes complete blockage (100% attenuation) by building structures, even though the actual attenuation will vary according to the building material. Third, the attenuation of RF signals in the GNSS band by vegetation varies with plant species, foliage dryness and seasonal foliage thickness [22]. Foliage at both sites is comprised of several species. In this initial report, winter recordings are not separated from recordings in other seasons, and while a cursory comparison of results derived from those recordings (not shown) reveals no seasonal difference in the characteristic attenuation curve, with more careful analysis such a difference may be detectable.

There are inherent errors in surveys of buildings and foliage. Foliage and buildings change over time, and survey measurements capture only a snapshot in time, so that the presence of an obstruction can only be surmised. Positional error in survey lidar, which arises in assigning coordinates from known surveyed points to corresponding locations in the lidar point cloud, is typically in the centimeter range.

Representational error arises from the spatial sampling and binning of a lidar point cloud to construct a 3D voxel array. This quantization error [27] may shift the alignment of obstructions with respect to the GNSS signal path. Errors of this sort will be more significant at low opacities. This is because low-opacity rays commonly intersect few voxels and so spurious samples form a high proportion of opacities summed along the ray. We suspect that much of the noise at low opacities seen in Figure 6 arises from spatial quantization error.

The receiver antenna sensitivity is not uniform. The manufacturer specification for the antenna (Onshine ANT-555) notes a 12dB difference between signals at 90° to the antenna and signals near the horizon. The satellite elevation and the UAV roll and pitch can be used to correct this systematic distortion in signal strength. While our analysis scripts can retrieve the UAV roll and pitch from the autopilot logs, this source of error is not corrected in the preliminary results shown.

Finally, this method relies on a known receiver position as the origin of the ray to trace to each satellite. This method is most reliable for preflight planning (e.g., Figure 5), wherein GNSS availability is forecast for an expected position at a specific time in the near future. Forecasts are limited to the near future since satellite orbit projections repositories only extrapolate from the current positions to a point in time at which the extrapolation error is moderate [28].

For in-flight or post-flight analysis, the method is critically dependent on the accuracy of the onboard receiver position estimate. In a location free of obstruction, the single-ended GNSS position may be off ± 2 meters horizontally and ± 4 meters vertically (95% confidence level [29][30]). In degraded GNSS locations, the position estimate may be much more inaccurate. There are methods to mitigate this uncertainty. GNSS receiver modules employ Kalman and other filtering methods to improve position estimates using temporal continuity and physical constraints on receiver motion. Some GNSS modules and some downstream processors (such as the Pixhawk autopilot) fuse position and motion information from other sensors (e.g., accelerometers and barometers) to further improve position estimates. However, these filtering methods can compensate for a degraded or lost GNSS fix only briefly.

VI. Conclusion

The ubiquity of GNSS geolocation greatly simplifies navigation on land, at sea, and in traditional aircraft, and is largely taken for granted. With the rapid development and application of nontraditional aircraft that operate close to the ground, there is increasing demand for flight in corridors with low or no access to the satellite signals needed to navigate reliably and safely. Geologic and urban canyons are two obvious types of GNSS-degraded corridors. Arboreal canyons, which accommodate roads, pipelines, and transmission lines, can also suffer from poor GNSS reception.

Fortuitously, simultaneous with the development of low-altitude aviation, adoption of lidar survey methods is enabling the means to predict the severity of GNSS degradation in these canyons. By tracing rays from the desired flight location to the GNSS constellation and measuring blockage by objects as mapped by lidar surveys — raycasting — the means to safely choose when and where to fly is at hand. For 'hard' canyons of rock and steel, the raycasting is straightforward. Either the ray is blocked, or it is not. For arboreal canyons, raycasting results are not binary, as the degree of signal attenuation varies from insignificant to unusable, depending not only on the depth of blockage but also the type of vegetation, its moisture content, and whether it is leafed (spring, summer, fall) or bare (winter).

Currently there exist very few studies of vegetative attenuation of radio signals of any sort and no surveys that are useful for prediction of GNSS fidelity. Because of the economic need for low altitude flight in arboreal canyons, there is a compelling need to create such surveys. We have attempted in this study to show how such surveys can be conducted with low cost receivers and aircraft. We showed that the physics needed to characterize arboreal flight corridors is largely in place, and we described the data processing methods which apply that physics fruitfully.

References

[1] Roth, Scott D. "Ray casting for modeling solids." Computer graphics and image processing 18, no. 2 (1982): 109-144.

[2] Wang, Sidney W., and Arie E. Kaufman. "Volume-sampled 3D modeling." IEEE Computer Graphics and Applications 14, no. 5 (1994): 26-32.

[3] Cook, Robert L., Thomas Porter, and Loren Carpenter. "Distributed ray tracing." In ACM SIGGRAPH computer graphics, vol. 18, no. 3, pp. 137-145. ACM, 1984.

[4] Ray, Jayanta Kumar, and M. Elizabeth Cannon. "Characterization of GPS carrier phase multipath." In Proceedings of ION National Technical Meeting, pp. 243-252. 1999.

[5] Panicciari, Tommaso, Soliman, Mohamed Ali, Moura, Grégory, "Evaluation of a GNSS Receiver Performance in Different Multipath Environments with a Novel Real-time Multipath Simulation System," Proceedings of the 30th International Technical Meeting of The Satellite Division of the Institute of Navigation (ION GNSS+ 2017), Portland, Oregon, September 2017, pp. 427-435.

[6] Soloviev, Andrey, Bruckner, Dean, van Graas, Frank, Marti, Lukas, "Assessment of GPS Signal Quality in Urban Environments Using Deeply Integrated GPS/IMU," Proceedings of the 2007 National Technical Meeting of The Institute of Navigation, San Diego, CA, January 2007, pp. 815-828.

[7] Bauer, Sven, Marcus Obst, and Gerd Wanielik. "3D environment modeling for GPS multipath detection in urban areas." In International Multi-Conference on Systems, Signals & Devices, pp. 1-5. IEEE, 2012.

[8] Costa, Emanoel. "Simulation of the effects of different urban environments on GPS performance using digital elevation models and building databases." IEEE Transactions on Intelligent Transportation Systems 12, no. 3 (2011): 819-829.

[9] Obst, Marcus, Sven Bauer, and Gerd Wanielik. "Urban multipath detection and mitigation with dynamic 3D maps for reliable land vehicle localization." In Proceedings of the 2012 IEEE/ION Position, Location and Navigation Symposium, pp. 685-691. IEEE, 2012.

[10] Dill, Evan, Julian Gutierrez, Steven Young, Arthur Scholz, Emily Bates, Ken Schmitt, Jonathan Doughty and Andrew Moore, "A Predictive GNSS Performance Monitor for Autonomous Air Vehicles in Urban Environments," Proceedings of the ION GNSS+ 2021. St. Louis, Missouri, USA (2021)

[11] van Diggelen, Frank, "End Game for Urban GNSS: Googles Use of 3D Building Models," Inside GNSS, vol. 16, No. 2, March 21, 2021

[12] van Diggelen, Frank, and Jennifer Wang, "Android Developers Blog: Improving urban GPS accuracy for your app," Dec 7, 2020, retrieved 5/16/2021 from https://android-developers.googleblog.com/2020/12/improving-urban-gps-accuracy-for-your.html

[13] Lefsky, Michael A., Warren B. Cohen, Geoffrey G. Parker, and David J. Harding. "Lidar remote sensing for ecosystem studies: Lidar, an emerging remote sensing technology that directly measures the three-dimensional distribution of plant canopies, can accurately estimate vegetation structural attributes and should be of particular interest to forest, landscape, and global ecologists." BioScience 52, no. 1 (2002): 19-30.

[14] Matikainen, Leena, Matti Lehtomäki, Eero Ahokas, Juha Hyyppä, Mika Karjalainen, Anttoni Jaakkola, Antero Kukko, and Tero Heinonen. "Remote sensing methods for power line corridor surveys." ISPRS Journal of Photogrammetry and Remote Sensing 119 (2016): 10-31. Sensing 119 (2016): 10-31.

[15] Moore, Andrew, Matthew Schubert, and Nicholas Rymer. "Autonomous Inspection of Electrical Transmission Structures with Airborne UV Sensors and Automated Air Traffic Management." In 2018 AIAA Information Systems-AIAA Infotech@ Aerospace, p. 1628. 2018.

[16] Moore, Andrew J., Matthew Schubert, Nicholas Rymer, Swee Balachandran, Maria Consiglio, Cesar Munoz, Joshua Smith, Dexter Lewis, and Paul Schneider. "UAV Inspection of Electrical Transmission Infrastructure with Path Conformance Autonomy and Lidar-based Geofences NASA Report on UTM Reference Mission Flights at Southern Company Flights November 2016." NASA Technical Memo (2017): 2017-219673.

[17] Wolcott, Ryan W., and Ryan M. Eustice. "Visual localization within lidar maps for automated urban driving." In 2014 IEEE/RSJ International Conference on Intelligent Robots and Systems, pp. 176-183. IEEE, 2014

[18] Rusu, Radu Bogdan, and Steve Cousins. "3d is here: Point cloud library (pcl)." In 2011 IEEE international conference on robotics and automation, pp. 1-4. IEEE, 2011.

[19] Crustal Dynamics Data Information System, https://cddis.nasa.gov/

[20] Moore, Andrew, Matthew Schubert, Terry Fang, Joshua Smith, and Nicholas Rymer. "Lidar-derived Navigational Geofences for Low Altitude Flight Operations." In AIAA AVIATION 2020 FORUM, p. 2908. 2020.

[21] Young, Steven, Ersin Ancel, Andrew Moore, Evan Dill, Cuong Quach, John Foster, Kaveh Darafsheh et al. "Architecture and Information Requirements to Assess and Predict Flight Safety Risks During Highly Autonomous Urban Flight Operations," NASA Technical Memo 2020-220440 (2020).

[22] Attenuation in Vegetation ITU-R Recommendation P833-9, Geneva, September 2016.

[23] Wright, William C. "Quantifying Global Position System signal attenuation as a function of three-dimensional forest canopy structure." PhD diss., University of Florida, 2008.

[24] Wright, William, Benjamin Wilkinson, and Wendell Cropper. "Development of a GPS forest signal absorption coefficient index." Forests 9, no. 5 (2018): 226.

[25] Spilker Jr, James J., Penina Axelrad, Bradford W. Parkinson, and Per Enge, eds. Global positioning system: theory and applications, volume I. American Institute of Aeronautics and Astronautics, 1996.

[26] https://github.com/rinex20/RTKLIB-demo5

[27] Widrow, Bernard, and István Kollár. "Quantization noise." Cambridge University Press 2 (2008): 5

[28] Seppänen, M., Ala-Luhtala, J., Piché, R., Martikainen, S. and Ali-Löytty, S., 2012. Autonomous prediction of GPS and GLONASS satellite orbits. NAVIGATION: Journal of the Institute of Navigation, 59(2), pp.119-134.

[29] Civil Report Card On GPS Performance Nov 2017. (2017, December). Retrieved March 15, 2018, from http://www.nstb.tc.faa.gov/reports/ReportCards/2017%2011.pdf

[30] Renfro, B., Jessica Rosenquest, Audric Terry, and Nicholas Boeker. "An Analysis of Global Positioning System (GPS) Standard Positioning System (SPS) Performance for 2015." Space and Geophysics Laboratory. Applied Research Laboratories. The University of Texas at Austin (2017).